LETTER

Combinatorial design of textured mechanical metamaterials

Corentin Coulais[1,2], Eial Teomy[3], Koen de Reus[1], Yair Shokef[3] & Martin van Hecke[1,2]

The structural complexity of metamaterials is limitless, but, in practice, most designs comprise periodic architectures that lead to materials with spatially homogeneous features[1–11]. More advanced applications in soft robotics, prosthetics and wearable technology involve spatially textured mechanical functionality, which requires aperiodic architectures. However, a naive implementation of such structural complexity invariably leads to geometrical frustration (whereby local constraints cannot be satisfied everywhere), which prevents coherent operation and impedes functionality. Here we introduce a combinatorial strategy for the design of aperiodic, yet frustration-free, mechanical metamaterials that exhibit spatially textured functionalities. We implement this strategy using cubic building blocks—voxels—that deform anisotropically, a local stacking rule that allows cooperative shape changes by guaranteeing that deformed building blocks fit together as in a three-dimensional jigsaw puzzle, and three-dimensional printing. These aperiodic metamaterials exhibit long-range holographic order, whereby the two-dimensional pixelated surface texture dictates the three-dimensional interior voxel arrangement. They also act as programmable shape-shifters, morphing into spatially complex, but predictable and designable, shapes when uniaxially compressed. Finally, their mechanical response to compression by a textured surface reveals their ability to perform sensing and pattern analysis. Combinatorial design thus opens up a new avenue towards mechanical metamaterials with unusual order and machine-like functionalities.

The architecture of a material is crucial for its properties and functionality. This connection between form and function is leveraged by mechanical metamaterials[1–15], whose patterned microstructures are designed to obtain unusual behaviours such as negative response parameters[1,9], multistability[5,8,11] or programmability[8,12]. For ordinary materials, aperiodic architectures and structural complexity are associated with geometric frustration[16,17], which prevents a coherent and predictable response. Frustration hinders functionality, and metamaterial designs have therefore focused on periodic structures. However, the high level of control provided by 3D printing provokes the question of whether one can design and create structurally complex, yet frustration-free, metamaterials[18].

We investigate this question using a combinatorial design strategy. We assemble 1-cm^3 flexible, cubic building blocks, or voxels, into a cubic lattice that then forms a metamaterial (Fig. 1a). These building blocks are anisotropic and have one soft mode of deformation aligned with their internal axis of orientation, resulting in elongated or flattened shapes that we refer to as 'bricks' with positive or negative polarization (Fig. 1b). Generally, mechanical metamaterials with randomly oriented building blocks are frustrated, because it is impossible for all blocks to cooperatively deform according to their soft mode: the bricks do not fit. We call voxelated[19] metamaterials that allow soft deformations, or, equivalently, in which all bricks fit, 'compatible'. A trivial example of a compatible configuration is a periodic stacking of alternately polarized, parallely orientated bricks. Hence, a periodic metamaterial consisting of parallel blocks is expected to exhibit a collective and harmonious deformation mode. We realized such a metamaterial by a combination of 3D printing and moulding (see Methods). Uniaxial compression indeed triggers a collective pattern change[2] in three dimensions and produces the expected staggered configuration in which each brick is adjacent to six bricks of opposite polarization (Fig. 1c; Supplementary Video 1).

We now consider the way in which to design aperiodic, yet frustration-free, mechanical metamaterials. Crucially, the internal structure of our blocks is anisotropic and each block can be oriented independently to allow structurally complex architectures. We think of these blocks as voxels, represent their orientation at each lattice point with a colour (Fig. 1d) and explore the discrete design space of such voxelated metamaterials. Compatibility requires two conditions to be met. First, pairs
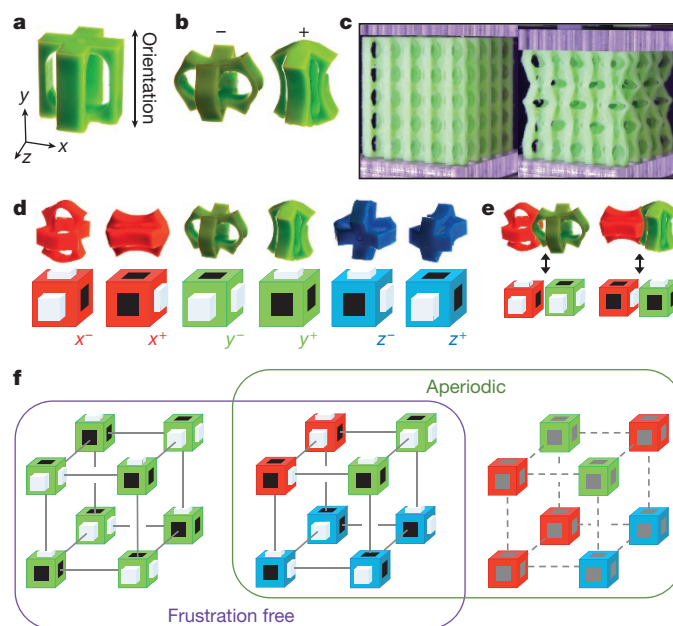

Figure 1 | Voxelated mechanical metamaterials. a, A flexible anisotropic building block in its undeformed state. **b,** Corresponding flattened (−) and elongated (+) deformed bricks. **c,** A 5 × 5 × 5 metacube consisting of parallel blocks (left) shows a collective deformation under uniaxial compression (right). **d,** Bricks (top) and their schematic representation (bottom), with the colour indicating orientation, and black dents and white protrusions representing deformations. **e,** Two examples where appropriately polarized, adjacent bricks fit together. **f,** Periodic (left), complex (middle) and frustrated (right) 2 × 2 × 2 stackings—for the frustrated stacking, no consistent brick configurations exist (grey/dashed). Schematic symbols are separated from one another for ease of visualization.

[1]Huygens-Kamerlingh Onnes Laboratory, Universiteit Leiden, PO box 9504, 2300 RA Leiden, The Netherlands. [2]FOM Institute AMOLF, Science Park 104, 1098 XG Amsterdam, The Netherlands. [3]School of Mechanical Engineering and The Sackler Center for Computational Molecular and Materials Science, Tel Aviv University, Tel Aviv 69978, Israel.
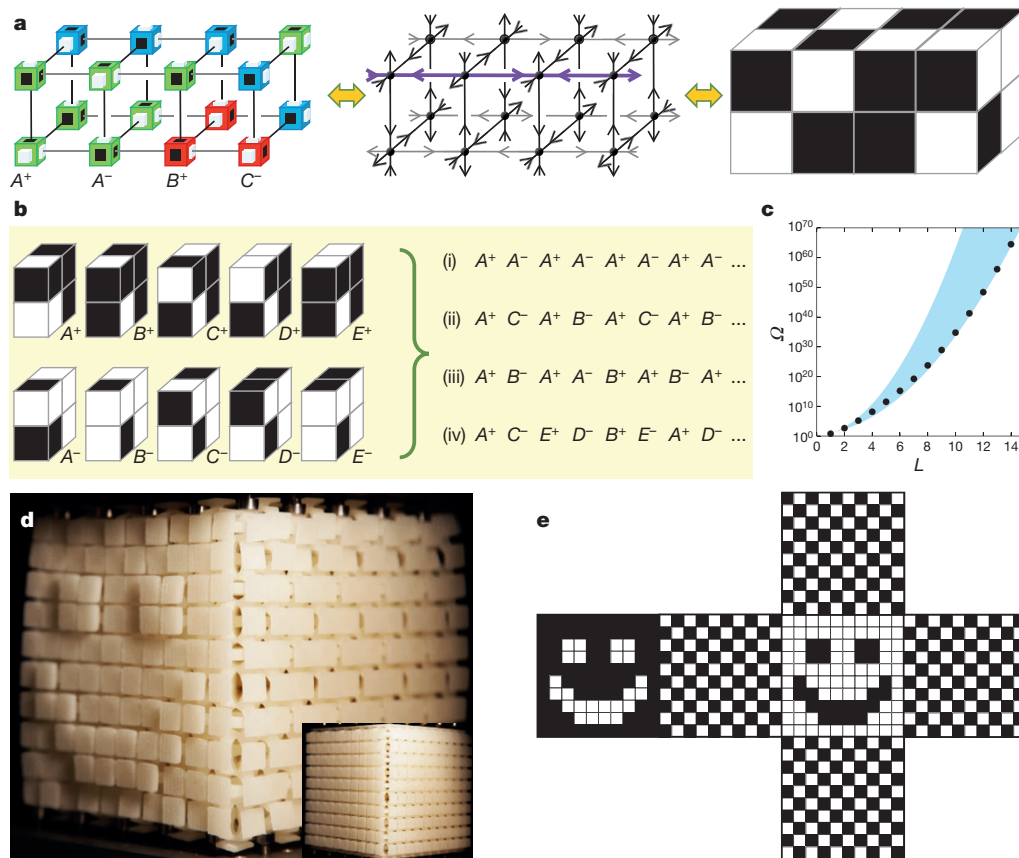
Figure 2 | Combinatorial design. a, Mapping of bricks to internal spins and then to surface spins (from left to right). **b**, Set of five pairs of motifs compatible with a given x texture, and examples of periodic (i, ii), quasi-periodic (iii; beginning of the Fibonacci sequence) and aperiodic (iv) motif stackings. **c**, Exact number of compatible $L \times L \times L$ spin configurations Ω (black circles) and lower and upper bounds (blue shaded region); see Methods and Supplementary Information. **d**, A $10 \times 10 \times 10$ metacube reveals its precisely designed surface texture under uniaxial compression. Square surface pedestals added for visualization. Inset, the undeformed metacube. See Methods for experimental details and Supplementary Videos 2–4. **e**, Schematic representation of the deformations at all surfaces of the metacube in **d**.

of neighbouring bricks should exhibit closely matching shapes along their common face. Our building blocks are precisely designed such that, given the polarization of one brick, the polarization of an adjacent brick can be adapted so that the pair have a tight fit, irrespective of their mutual orientation. Hence, we need to track only the outward or inward deformations of the surfaces of the building blocks (Fig. 1e). The second compatibility condition concerns the combinatorics of the voxel arrangement: all bricks should fit, such that protrusions and depressions of all neighbouring bricks are matched. In general, the first condition can be met by clever building-block design, whereas the second condition leads to a complex combinatorial 3D tiling problem.

As we will show, although the compatibility condition is violated in most random configurations, which are consequently frustrated, our specific building blocks allow for many complex configurations where all protrusions and depressions match. These non-parallel, structurally complex, yet compatible, architectures combine the rich spatial texture of aperiodic materials with the predictability of ordered materials, and form the blueprint for aperiodic, frustration-free mechanical metamaterials (Fig. 1f).

The design of complex architectures is simplified by mapping brick configurations to spin configurations that satisfy a so-called 'ice rule'[20–23] and, as such, is reminiscent of tiling[24] and constraint-satisfaction[25,26] problems. We identify each brick with a vertex, connected to neighbouring vertices by bonds that represent the common face between bricks (Fig. 2a). Dents and bumps map to inward or outward spins σ_x, σ_y, σ_z, and by placing a single spin per bond, the first compatibility condition is trivially satisfied. The second condition maps to the ice rule,

which stipulates that the six bonds of each vertex should correspond to a brick configuration, whereby the six bricks, x^-, x^+, y^-, y^+, z^- and z^+, correspond to spin configurations $(\sigma_x, \sigma_y, \sigma_z) = (-++)$, $(+--)$, $(+-+)$, $(-+-)$, $(++-)$ and $(--+)$, respectively. Evidently, each allowed spin configuration corresponds to a compatible brick stacking and corresponding voxel configuration. Conversely, each compatible voxel configuration corresponds to two spin configurations related by parity (spin flip)—a symmetry that originates from the opposite polarizations allowed by each building block.

All compatible metamaterials thus obtained feature an unusual form of long-range order that relates the boundary to the bulk. Owing to the reflection symmetry of the bricks, spins along lines of bonds are alternating. Therefore, spins at opposing boundaries are equal (opposite) when their distance is odd (even). Because spins at the surface of a metamaterial represent its texture of bumps and dents, this property implies that textures at opposite faces of a metacube are directly linked. Moreover, once the surface texture is fixed, all internal spins and therefore bricks are determined (Fig. 2a). We call this unusual relation between surface and bulk 'holographic order' (see Methods).

The combination of parity and holographic order implies that any motif consisting of $n \times p \times q$ compatible blocks can be stacked in a space-filling manner, because the surface spins of such motifs have compatible textures. Moreover, once the x spins are fixed along a plane, we can determine a set containing all motifs A^+, B^+, … with matching x spins and by parity obtain A^-, B^-, … (Fig. 2b and Methods). These motifs can be stacked in an arbitrary order, as long as we alternate between '+' and '−' motifs; this allows the straightforward design of periodic, quasi-periodic and aperiodic metamaterials (Fig. 2b).
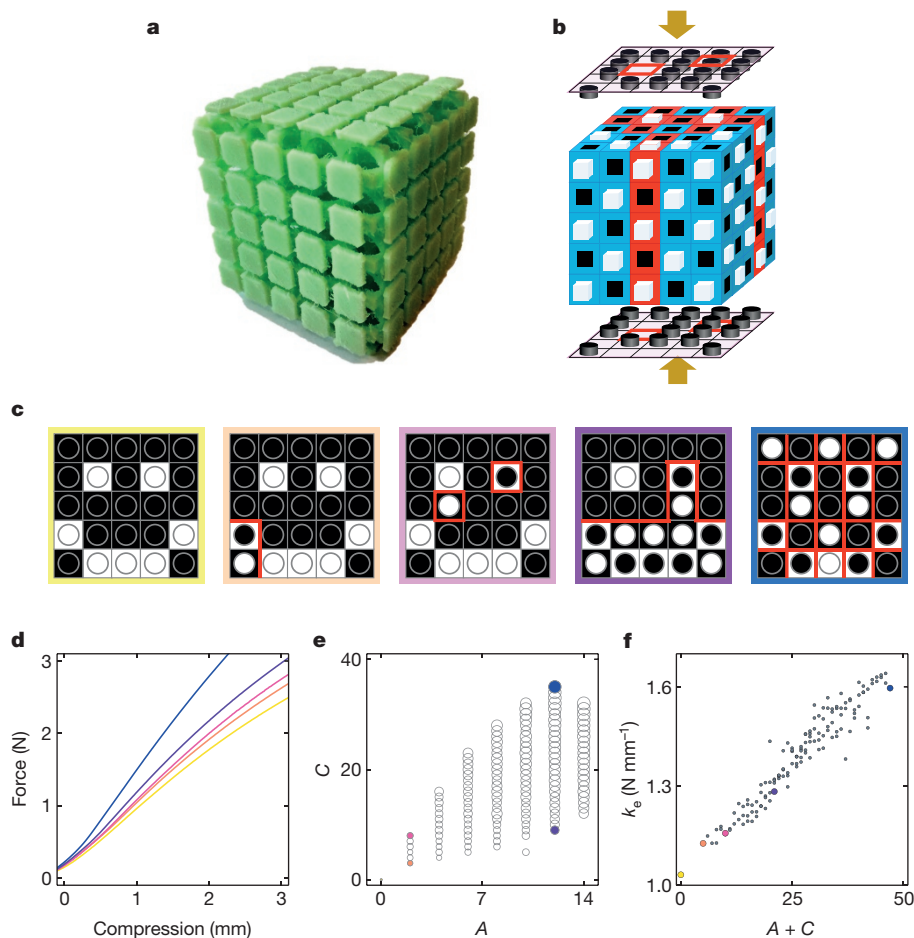
Figure 3 | Pattern recognition and pattern analysis. a, Experimental realization of an elastic $5 \times 5 \times 5$ metacube programmed for a 'smiley' texture. **b**, Schematic of experiments where the metacube in **a** is compressed between patterned clamps. The red and blue building blocks are oriented as in Fig 1; cylinders signify stubs that are positioned at sites where $\sigma_z^K = 1$ and red lines demarcate regions where $\sigma_z^K = \sigma_z^L$ and $\sigma_z^K = -\sigma_z^L$. **c**, Examples of mismatch between cube lock texture $\{\sigma_z^L\}$ (squares) and boundary key textures $\{\sigma_z^K\}$ (circles). Red lines as in **b**.

d, Experimental force–compression curves. Colour corresponds to the key textures in **c**. **e**, The experimentally obtained stiffness k_e varies systematically with both the area (A) and circumference (C) of the mismatch. Coloured data points correspond to the key textures in **c**, and the size of each circle represents k_e (the yellow data point at $A = C = 0$ corresponds to very small k_e and so is hard to see). **f**, The stiffness k_e is essentially linear in $A + C$. Coloured data points as in **e**; small filled grey circles correspond to the open circles in **e**.

By removing building blocks at the boundary, complex shapes can be realized; but for simplicity we focus here on cubic metamaterials.

Holographic order substantially restricts the number of potential compatible configurations: whereas for generic configurations their multitude is set by the volume, for compatible configurations it is set by the surface area. Moreover, many surface textures lead to forbidden internal vertices such as where all spins are equal. For example, in general it is not possible to arbitrarily choose the surface texture at two faces simultaneously. Nevertheless, the number of distinct $L \times L \times L$ (equivalent to $n \times p \times q$, above, with $n = p = q := L$) spin configurations $\Omega(L)$ is extremely large. To quantify the design limits and possibilities, we exactly evaluated $\Omega(L)$ up to $L = 14$ where $\Omega \approx 3 \times 10^{64}$, and obtained strict and asymptotic lower and upper bounds (Fig. 2c, Methods and Supplementary Information).

Despite the limitations imposed by compatibility, the design space of voxelated metamaterials is huge. To illustrate this, we constructed a general algorithm to obtain all $L \times L \times 1$ motifs that are compatible with a given texture $\{\sigma_z\}$ (see Methods and Supplementary Information); for each texture there are at least two distinct motifs. We now show that we can use this algorithm to design arbitrarily pixelated patterns of bumps and depressions, or textures, at a given surface of a metacube as a step towards arbitrary shape-morphing materials. In Fig. 2d we show a rationally designed metacube created by 3D printing. Under uniaxial

compression (see Methods), the initially flat surface of this cube reveals its spatial texture, with the front and back related by holography (Fig. 2e, Methods and Supplementary Videos 2–4). This cooperative, complex, yet controlled, shape morphing illustrates that our combinatorial method allows for the rational design of shape-shifting metamaterials.

We finally show that when aperiodic metacubes are compressed by patterned surfaces their response can be used for mechanical pattern analysis. We created a compatible $5 \times 5 \times 5$ metacube, programmed with a 'smiley' texture $\pm \{\sigma_z^L\}$ that acts as a 'lock' (see Methods), which is compressed between two identical surfaces that have a pixelated 'key' texture $\{\sigma_z^K\}$, created by placing 18 stubs in templated clamps (Fig. 3a, b). We characterize the difference between lock and key patterns by the area or number of misplaced stubs, A, as well as the circumference of the misplaced area, C (Fig. 3c), and use 136 different key patterns, which cover all possible values of A and C that can be reached by 18 stubs. For each key, we performed experiments (simulations) to determine the stiffness k_e (k_s) via the slope of the force–compression curves—the values agree very closely with one another (see Methods). When the key equals one of the two lock textures $\pm \{\sigma_z^L\}$, all bricks deform compatibly and the stiffness k is low. Incompatibly textured surfaces push metacubes into frustrated states, leading to an energy penalty and increased stiffness (Fig. 3d). The increase with A evidences

simple lock-and-key functionality, but when *k* is plotted as function of *A* and *C*, it is seen to increase with *C* also—for the same number of misplaced stubs, a range of stiffnesses can be observed (Fig. 3e). When plotted as function of $A + C$, all our data collapse onto a straight line, which evidences intricate collective phenomena (Fig. 3f). We suggest that, owing to parity, different parts of the cube deform in opposing parity, and that the stiffness is determined by the size of the domain walls separating these regions, which is given by $A + C$ (see Methods). Together, these findings demonstrate the ability of a metacube to perform an arithmetical calculation on the mismatch between key and lock patterns, in behaviour more readily associated with machines than with materials.

Combinatorial strategies enable the design of machine-like materials that can be programmed with specific shape-sensing and shape-shifting tasks. We anticipate that combinatorial design of textured metamaterials can be extended in various directions. First, the inclusion of vacancies could lead to multishape materials[27], whereas defects can induce controlled frustration to obtain multistability, memory and programmability[8,11,12]. Second, differently shaped building blocks, such as triangles or hexagons in two dimensions and truncated octahedra or gyrobifastigii in three dimensions, or mixtures of building blocks could be used to tile space. Third, building blocks with degrees of freedom that are different from the simple 'inwards or outwards' deformations considered here could be considered—a prime example being origami units that have folding motions[10–12]. Finally, heating or magnetic fields instead of compression could be used to actuate shape-changing metamaterials, while non-mechanical textured functionalities such as wavefront shaping could also be achieved. We envision a range of applications for which control and processing of spatially complex mechanical information is key. Textured metamaterials can be designed to naturally interface with the complex shapes and shapeability of the human body, in prosthetics, haptic devices and wearables. Moreover, shape changing is central to a wide variety of actuators and sensors, in particular in the context of soft robots[28–30]. Finally, at smaller scales, controllable surface textures could control friction, wetting and drag.

1. Lakes, R. Foam structures with a negative Poisson's ratio. *Science* **235,** 1038–1040 (1987).
2. Mullin, T., Deschanel, S., Bertoldi, K. & Boyce, M. C. Pattern transformation triggered by deformation. *Phys. Rev. Lett.* **99,** 084301 (2007).
3. Grima, J. N. & Evans, K. E. Auxetic behavior from rotating squares. *J. Mater. Sci. Lett.* **19,** 1563–1565 (2000).
4. Schaedler, T. A. *et al.* Ultralight metallic microlattices. *Science* **334,** 962–965 (2011).
5. Nicolaou, Z. G. & Motter, A. E. Mechanical metamaterials with negative compressibility transitions. *Nat. Mater.* **11,** 608–613 (2012).
6. Babaee, S., Shim, J., Weaver, J. C., Patel, N. & Bertoldi, K. 3D soft metamaterials with negative Poisson's ratio. *Adv. Mater.* **25,** 5044–5049 (2013).
7. Kadic, M., Bückmann, T., Schittny, R. & Wegener, M. Metamaterials beyond electromagnetism. *Rep. Prog. Phys.* **76,** 126501 (2013).
8. Florijn, B., Coulais, C. & van Hecke, M. Programmable mechanical metamaterials. *Phys. Rev. Lett.* **113,** 175503 (2014).
9. Coulais, C., Overvelde, J. T. B., Lubbers, L. A., Bertoldi, K. & van Hecke, M. Discontinuous buckling of wide beams and metabeams. *Phys. Rev. Lett.* **115,** 044301 (2015).
10. Schenk, M. & Guest, S. D. Geometry of Miura-folded metamaterials. *Proc. Natl Acad. Sci. USA* **110,** 3276–3281 (2013).
11. Waitukaitis, S., Menaut, R., Chen, B. G. & van Hecke, M. Origami multistability: from single vertices to metasheets. *Phys. Rev. Lett.* **114,** 055503 (2015).
12. Silverberg, J. L. *et al.* Using origami design principles to fold reprogrammable mechanical metamaterials. *Science* **345,** 647–650 (2014).
13. Bückmann, T., Thiel, M., Kadic, M., Schittny, R. & Wegener, M. An elasto-mechanical unfeelability cloak made of pentamode metamaterials. *Nat. Commun.* **5,** 4130 (2014).
14. Paulose, J., Meeussen, A. S. & Vitelli, V. Selective buckling via states of self-stress in topological metamaterials. *Proc. Natl Acad. Sci. USA* **112,** 7639–7644 (2015).
15. Liu, Z. *et al.* Locally resonant sonic materials. *Science* **289,** 1734–1736 (2000).
16. Wannier, G. H. Antiferromagnetism: the triangular Ising net. *Phys. Rev.* **79,** 357–364 (1950).
17. Sadoc, J. F. & Mosseri, R. *Geometrical Frustration* (Cambridge Univ. Press, 1999).
18. Zykov, V., Mytilinaios, E., Adams, B. & Lipson, H. Robotics: Self-reproducing machines. *Nature* **435,** 163–164 (2005).
19. Ware, T. H., McConney, M. E., Wie, J. J., Tondiglia, V. P. & White, T. J. Voxelated liquid crystal elastomers. *Science* **347,** 982–984 (2015).
20. Harris, M. J., Bramwell, S. T., McMorrow, D. F., Zeiske, T. & Godfrey, K. W. Geometrical frustration in the ferromagnetic pyrochlore $Ho_2Ti_2O_7$. *Phys. Rev. Lett.* **79,** 2554–2557 (1997).
21. Wang, R. F. *et al.* Artificial 'spin ice' in a geometrically frustrated lattice of nanoscale ferromagnetic islands. *Nature* **439,** 303–306 (2006).
22. Castelnovo, C., Moessner, R. & Sondhi, S. L. Magnetic monopoles in spin ice. *Nature* **451,** 42–45 (2008).
23. Nisoli, C., Moessner, R. & Schiffer, P. *Colloquium*: Artificial spin ice: designing and imaging magnetic frustration. *Rev. Mod. Phys.* **85,** 1473–1490 (2013).
24. Grünbaum, B. & Shephard, G. C. *Tilings and Patterns* (Freeman, 1987).
25. Kirkpatrick, S., Gelatt, C. D. Jr & Vecchi, M. P. Optimization by simulated annealing. *Science* **220,** 671–680 (1983).
26. Mezard, M., Parisi, G. & Virasoro, M. A. *Spin Glass Theory and Beyond* (World Scientific, 1987).
27. Cho, Y. *et al.* Engineering the shape and structure of materials by fractal cut. *Proc. Natl Acad. Sci. USA* **111,** 17390–17395 (2014).
28. Leong, T. G. *et al.* Tetherless thermobiochemically actuated microgrippers. *Proc. Natl Acad. Sci. USA* **106,** 703–708 (2009).
29. Shepherd, R. F. *et al.* Multigait soft robot. *Proc. Natl Acad. Sci. USA* **108,** 20400–20403 (2011).
30. Overvelde, J. T., Kloek, T., Dhaen, J. J. & Bertoldi, K. Amplifying the response of soft actuators by harnessing snap-through instabilities. *Proc. Natl Acad. Sci. USA* **112,** 10863–10868 (2015).

METHODS

Combinatorial design. The presence of holographic order reduces the number of potential compatible $L \times L \times L$ spin configurations from $2 \times 3^{L^3}$ (L^3 blocks with 3 orientations and parity) to 2^{3L^2} (3 pairs of opposing surfaces each with L^2 spins). The vast majority of these are not compatible and to better understand our design space, we discuss how to exactly evaluate and obtain upper and lower bounds for $\Omega(L)$—the number potentially compatible $L \times L \times L$ spin configurations. We construct cubes by stacking motifs, and Q counts the number of $L \times L \times 1$ motifs compatible with a given texture $\{\sigma_z\}$.

To understand the possible motifs, we now classify the patterns of z bricks that arise in $L \times L \times 1$ motifs. Crucially, z bricks are sources or sinks for the in-plane spins σ_x and σ_y, and therefore each 2×2 submotif can contain only 0, 2 or 4 z bricks. This restricts the patterns of z bricks to columns, rows, and intersecting columns and rows. In general, we can enumerate the patterns of z bricks using binary column and row vectors with elements c_i and r_j, respectively, and placing a z brick at location (i, j) only when $c_i \neq r_j$ (Extended Data Fig. 1a). On the z-bricks, the z-spins form checkerboard patterns, whereas the spins in the remainder of the pattern can be chosen at will by filling each position with either an x or y brick.

In the absence of z bricks, we can obtain two motifs by fixing σ_x and σ_y to be opposite and alternating; that is, at site (i, j) of the motif, $\sigma_x = -\sigma_y = (-1)^{i+j}$ or $\sigma_x = -\sigma_y = (-1)^{i+j+1}$. In both cases, each vertex is compatible with either an x or a y brick, with corresponding positive or negative σ_z. This allows the straightforward design of two $L \times L \times 1$ motifs consistent with any $\{\sigma_z\}$. In Extended Data Fig. 1b we show these motifs, as well as four more that are compatible with a 5×5 smiley texture; hence, $Q = 6$ for this texture. In principle, $\Omega(L)$ can be exactly evaluated by determining Q for each texture $\{\sigma_z\}$, and then summing over all textures (see Supplementary Information and Extended Data Fig. 1c): $\Omega(L) := \sum_{\sigma_z} Q^L$.

Lower bound. A lower bound for Ω follows from our construction to create two motifs for any spin configuration, which implies that $Q \geq 2$. As these can be stacked in an arbitrary order, this yields at least 2^L spin configurations for a given texture. Because there are 2^{L^2} σ_z textures, we find that $\Omega(L) \geq 2^{L^2+L}$.

Staggered spins. To simplify the counting of the number of compatible spin configurations $\Omega(L)$ (for details see Supplementary Information), we define staggered spins $\tilde{\sigma}$, such that for site (i, j, k) in the metacube $\tilde{\sigma}_\alpha^{(i,j,k)} = (-1)^{i+j+k} \sigma_\alpha^{(i,j,k)}$, for $\alpha = x, y, z$. Under this invertible transformation, a checkerboard texture of $\{\sigma_z\}$, for example, corresponds to a homogeneous texture of $\{\tilde{\sigma}_z\}$ where all staggered spins are equal to either $+1$ or -1. Moreover, all sites in a given row, column or tube have the same value of $\tilde{\sigma}_x$, $\tilde{\sigma}_y$ or $\tilde{\sigma}_z$, respectively.

Upper bound. For a simple upper bound we note that the maximum value of Q is obtained when $\tilde{\sigma}_z \equiv +1$ or $\tilde{\sigma}_z \equiv -1$. For each of these textures there are $Q = 2^{L+1} - 1$ spin configurations. Consider, for example, $\tilde{\sigma}_z \equiv +1$. If $\tilde{\sigma}_z \equiv -1$, then all the $\tilde{\sigma}_y$ are free, leading to 2^L compatible structures; if $\tilde{\sigma}_y \equiv -1$, then all the $\tilde{\sigma}_x$ are free, leading to an additional 2^L compatible structures. Because $\tilde{\sigma}_x \equiv \tilde{\sigma}_y \equiv -1$ was counted twice, the total number is $2^L + 2^L - 1 = 2^{L+1} - 1$. Hence, we obtain as an upper bound: $\Omega(L) \leq 2^{L^2}(2^{L+1} - 1)^L < 2^{2L^2+L}$. A stricter upper bound is derived in Supplementary Information: $\Omega(L) \leq 4L \times (3/4)^L \times 2^{2L^2}$. The exact evaluation of $\Omega(L)$ is explained in Supplementary Information and the results are given in Extended Data Table 1.

Design limits. We note here that if n is the number of pairs of opposing surfaces where the spins can be chosen freely, then $\Omega(L) \approx 2^{nL^2}$, and that the simple lower and upper bounds given above roughly correspond to $n = 1$ and $n = 2$. Approximate calculations detailed in Supplementary Information lead to $2^{L^2+L+\log_2(3)} \leq \Omega \leq 2^{L^2+2L+2}$, and our exact evaluation of $\Omega(L)$ shows that, for large L, Ω is quite close to the lower bound (Fig. 2a). Hence, once the texture of one surface is fixed, there is limited freedom, apart from the stacking order of motifs, to design textures at other surfaces. For most spin textures, only the two simple motifs are compatible and z bricks play a minor role.

Materials and fabrication. We created the $5 \times 5 \times 5$ specimens by 3D printing water-soluble moulds, in which we cast a well-calibrated silicon rubber (PolyvinylSiloxane, Elite Double 32, Zhermarck, Young's modulus, $E = 1.32$ MPa;

Poisson's ratio, $\nu \approx 0.5$). The unit bricks measure $11.46\,\text{mm} \times 11.46\,\text{mm} \times 11.46\,\text{mm}$, with a spherical pore of diameter $D = 10.92\,\text{mm}$ in the centre and four cuboid inclusions of dimension $4.20\,\text{mm} \times 4.20\,\text{mm} \times 11.46\,\text{mm}$ at the x and y corners; see Extended Data Fig. 2a. They are stacked with a pitch of $a = 11.46\,\text{mm}$, such that the filaments between the unit cells have a non-homogeneous cross-section with a minimal width $d = 0.54\,\text{mm}$ and a depth $w = 3.6\,\text{mm}$; see Extended Data Fig. 2b.

The $10 \times 10 \times 10$ sample has the same brick dimensions and was 3D printed commercially (Materialise, Leuven, Belgium) out of sintered polyurethane ($E \approx 14$ MPa). On the faces of the aperiodic cubes, square pedestals were added to facilitate visualization of the surface texture and compression by textured boundaries.

Mechanical tests. We compressed both metacubes at a rate of $0.02\,\text{mm s}^{-1}$ in a uniaxial testing device (Instron type 5965), which controls the compressive displacement u to better than $10\,\mu\text{m}$ and measures the compressive force with an accuracy of 10^{-4} N at an acquisition rate of 0.5 Hz.

Whereas we used flat plates for Fig. 1c, we used textured boundary conditions for Figs 2d and 3. We created textured top and bottom boundaries using aluminium plates with female 3-mm threads positioned in a square array of pitch $a = 11.46 \pm 0.02\,\text{mm}$, in which we mount stainless steel M3 screws whose caps were machined to a height of $3.50 \pm 0.01\,\text{mm}$ (see Extended Data Fig. 3a); this ensures precise levelling of the pins and flexibility in texture. At the start of each experiment, the cubes were carefully positioned and aligned by hand within a 1-mm accuracy on the bottom boundary. The screws were placed to form identical (complementary) top and bottom patterns for the $5 \times 5 \times 5$ ($10 \times 10 \times 10$) cube.

For the $10 \times 10 \times 10$ cube, designed as in Extended Data Fig. 4a, we used checkerboard textures that led to the desired pattern on one face (Fig. 2), the reverted pattern on the opposite face (Fig. 2 and Extended Data Fig. 4b) and checkerboard textures on the other faces (Fig. 2 and Extended Data Fig. 4c).

Numerical simulations. We probed the response of a $5 \times 5 \times 5$ aperiodic smiley metacube to different textures by performing a fully nonlinear analysis within the commercial package Abaqus/Standard. We modelled the elastomer using a neo-Hookean strain energy density with a Young's modulus of $E = 1.32$ MPa and a Poisson's ratio of $\nu = 0.4999$. We carried out a mesh optimization and a mesh density study leading to a typical mesh size of 0.6 mm and a total number of 1.5×10^6 hybrid quadratic tetrahedral elements (Abaqus type C3D10H). We applied uniaxial compression by applying 10 steps of magnitude $\Delta u = 0.25$ mm, using exactly the same boundary conditions and dimensions as in the experiments (Extended Data Fig. 5b).

Determination of k. The numerical force–displacement (F–u) curves are very well fitted by the quadratic form $F(u) = ku + \eta u^2$, which captures the effect of the nonlinear softening η and which allows an accurate estimation of the stiffness k. The experimental determination of the stiffness required special care, because small gravity-induced sagging of the cube causes a soft knee in the force–displacement curve when the top boundary makes contact with the sample. Therefore, we determined the stiffness by fitting the force–displacement curves to the same quadratic function as for the numerics, focusing on intermediate displacements $0.8\,\text{mm} \leq u \leq 2.5\,\text{mm}$ away from the knee where $\text{d}F/\text{d}u$ is linear in u; see Extended Data Fig. 5a.

Lock and key mechanics. For the lock-and-key experiments, we used a $5 \times 5 \times 5$ cube made by stacking five $B^\pm$ configurations (Extended Data Fig. 1b). The key patterns consisted of 18 screws placed in a 5×5 array (see Fig. 3b, c and Extended Data Fig. 3a, b). We focused on 136 configurations that have distinct values of the area A and circumference C of the texture mismatch. For experiments and simulations, we estimated the stiffness k and observe that it increases with the mismatch between lock and key. The variation of k in experiments and simulations closely match (Extended Data Fig. 5c). Neither A nor C are good predictors for the level of frustration. To interpret the outcome of the experiments with the $5 \times 5 \times 5$ cube, we posit that, for incompatible key textures, different parts of the cube approach compatible configurations with opposite parity, thus localizing the frustration along internal domain walls. Hence, a single misplaced pixel carries an energy penalty due to the four frustrated x and y sides of the brick in front of the defect, and one z side opposing the defect—when defects touch, their interface is not frustrated. Therefore, the size of the domain walls is equal to the number of frustrated sides, which is $A + C$.
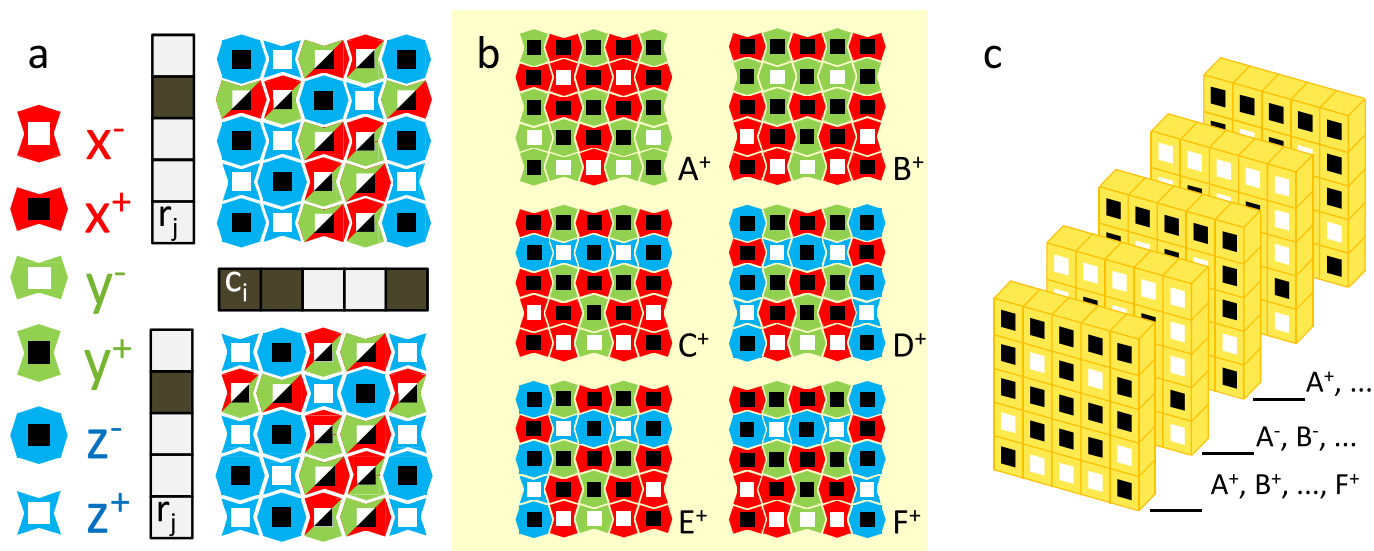
Extended Data Figure 1 | Motif-based design. a, 2D representation of the six bricks (x^-, x^+, y^-, y^+, z^-, z^+), and illustration of complex motifs. All complex motifs can be generated by defining two binary vectors with elements c_i (column) and r_j (row) that govern the placement of z bricks at location (i, j). The remaining sites are then filled with x and y bricks. Respecting parity, this generates all motifs for given c and r. **b**, The six motifs (A^+, …, F^+) that are compatible with a 5×5 smiley texture. **c**, A total of 6^5 smiley metacubes can be designed by varying the stacking order; here A^- denotes the same motif as A^+ but with inversed spins. The x and y spins follow from the choice of motifs.
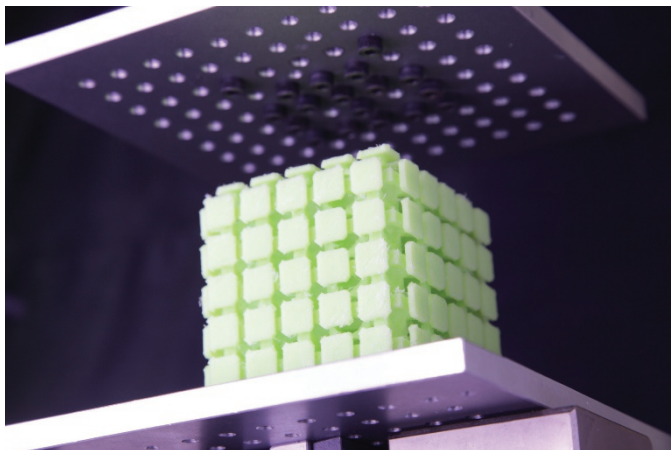
a

b
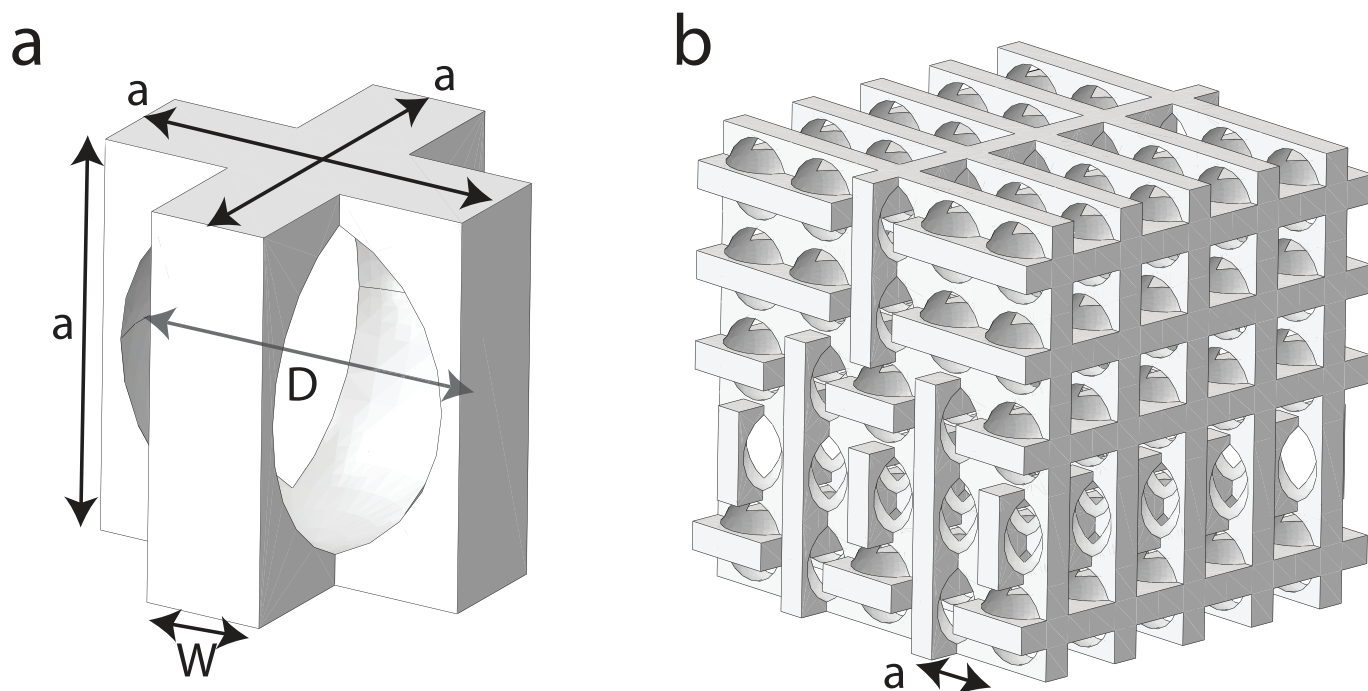
Extended Data Figure 2 | Implementation. a, **b**, Computer assisted design of the geometry of the unit cell (**a**) and a $5 \times 5 \times 5$ cube (**b**). All our samples were 3D printed with the dimensions $a = 11.46$ mm, $D = 10.92$ mm and $w = 3.6$ mm. To make the wall thickness outside the cube equal to the internal wall thickness, the outer walls are thickened by 0.27 mm.
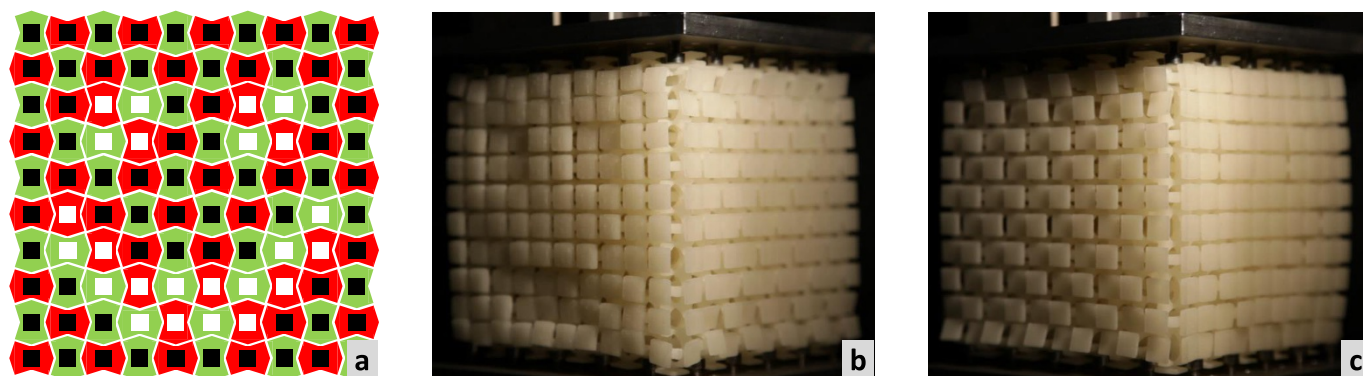
a

b
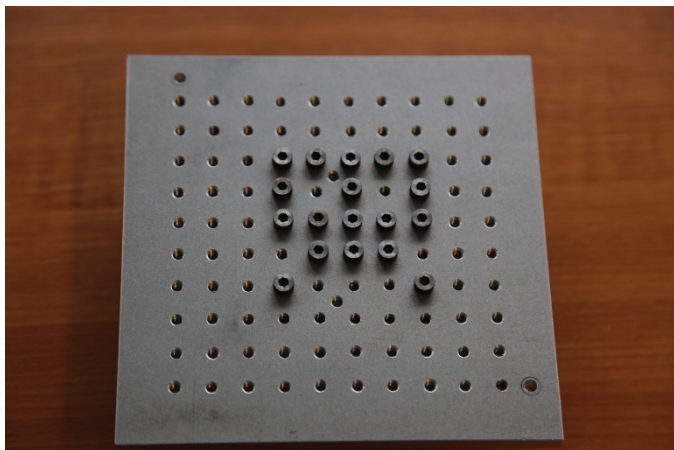
Extended Data Figure 3 | Lock-and-key experiment. a, Picture of the textured clamp. b, Side view of the experiment.

Extended Data Figure 4 | 10 × 10 × 10 metacube under uniaxial compression. a, Motif A^+—the cube is designed by stacking motifs A^+ and A^-. **b**, Opposite face of the one shown in Fig. 1e showing the inverted pattern. **c**, One of the transverse faces showing a checkerboard pattern.
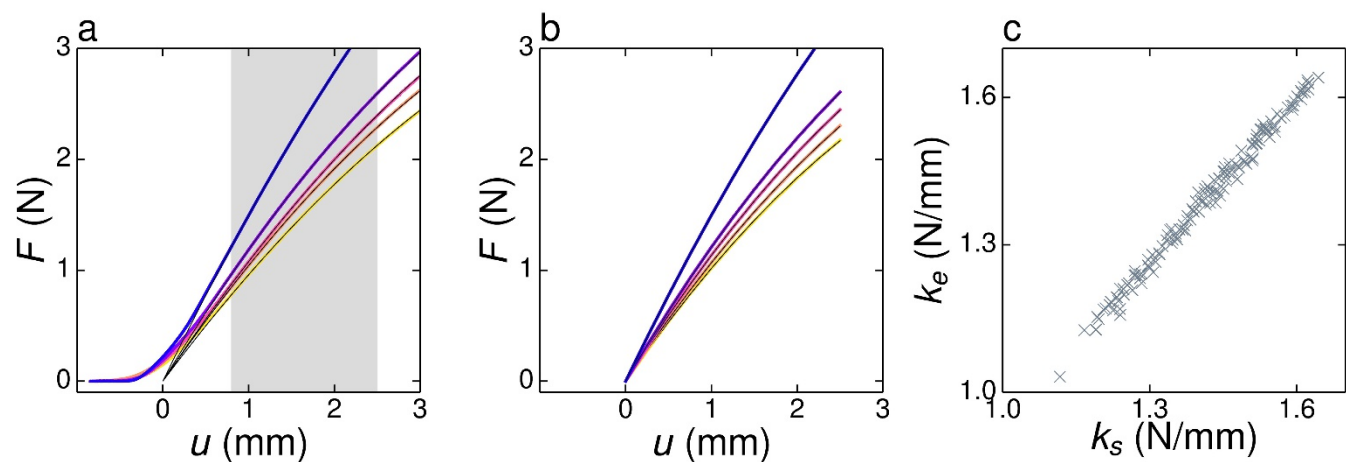
Extended Data Figure 5 | Complex sensory properties of a complex 5 × 5 × 5 metacube with internal smiley texture. a, Force–compression (F–u) curves for five experiments (thick solid lines), where the colour indicates the external texture shown in Fig. 3c. The black thin lines show fits with a quadratic function $F(u) = ku + \eta u^2$ performed in the shaded region $0.8\,\mathrm{mm} \le u \le 2.5\,\mathrm{mm}$. **b**, Corresponding numerical results. **c**, Scatter plot showing very good correspondence between the stiffness obtained from simulations (k_s) and experiments (k_e).

Extended Data Table 1 | The exact value of Ω for $L \times L \times L$ metacubes up to $L = 14$

L	Ω
1	6
2	450
3	151,206
4	145,456,074
5	325,148,366,166
6	1,562,036,085,226,890
7	17,234,732,991,509,112,246
8	578,304,084,367,752,824,053,674
9	84,438,573,424,284,282,414,882,546,966
10	58,592,971,553,875,504,020,753,814,442,326,410
11	181,442,224,689,012,470,542,563,031,429,841,423,983,926
12	2,404,888,026,041,008,595,056,652,999,310,606,919,098,996,796,074
13	126,725,905,761,644,879,286,362,510,660,061,876,041,719,518,257,045,613,846
14	30,625,852,190,216,495,511,364,347,343,665,021,261,262,812,628,299,779,541,749,100,810